Empirical constraints on ice-cliff calving

Caroline Needell

caroline.needell@whoi.edu

Massachusetts Institute of Technology—Woods Hole Oceanographic Institute Joint Program in Oceanography/Applied Ocean Science and Engineering https://orcid.org/0000-0002-6796-6120

Catherine Walker

Woods Hole Oceanographic Institution https://orcid.org/0000-0003-4019-1000

Jeremy Bassis

University of Michigan https://orcid.org/0000-0003-2946-7176

Physical Sciences - Article

Keywords:

Posted Date: July 21st, 2025

DOI: https://doi.org/10.21203/rs.3.rs-7133627/v1

Additional Declarations: There is **NO** Competing Interest.

Empirical constraints on ice-cliff calving

Caroline Needell[1], Catherine C. Walker[2], Jeremy N. Bassis[3]
[1]MIT-WHOI Joint Program in Oceanography/Applied Ocean Science & Engineering, Cambridge, MA
[2]Department of Applied Ocean Physics and Engineering, Woods Hole Oceanographic Institution, Woods Hole, MA
[3]Department of Climate and Space Sciences and Engineering, University of Michigan, Ann Arbor, MI

Abstract

When calving cliffs at the margins of Earth's ice sheets are taller than a critical height, runaway ice retreat may be triggered in a mechanism called the marine ice-cliff instability[1,2]. However, this idea remains controversial, because tall cliffs for which this process applies have rarely been observed. Limited observations show that, consistent with the marine ice-cliff hypothesis, cliff heights rarely exceed ~100 m[3–7]. But these observations neither constrain rates of retreat nor the potential for tall cliffs to fail in a self-sustaining process, resulting in poorly-constrained parameterizations of the instability. Here we address this limitation by examining ice cliffs across Earth's major ice-sheet margins using laser altimetry and optical imagery. We show that cliffs taller than 100 m are rare but exist in diverse settings. Calving rates increase with cliff height and exceed existing parameterizations by up to a factor of 3, but we do not observe runaway retreat. Instead, we find that dynamic thinning combined with retreat into regions with small ice thickness gradients eventually suppresses ice-cliff growth. These results suggest that projections of future ice loss may significantly underestimate retreat by cliff-calving, but that the potential for instability will depend sensitively on quantities like ice thickness gradients, not solely on cliff heights as current parameterizations assume.

Main

Earth's ice sheets flow toward the ocean as glaciers and ice streams, terminating either in floating ice shelves or near-vertical ice cliffs[8,9]. Although the Greenland Ice Sheet (GrIS) has lost most of its floating ice tongues, the Antarctic Ice Sheet (AIS) maintains ice shelves along approximately two-thirds of its coastline[10]. The future loss of floating ice shelves combined with retreat into the thick continental interior may expose ice cliffs that structurally fail, collapsing under their own weight when they exceed a critical height above the waterline[1,2] (H_{crit}). This form of calving, known as ice-cliff failure or ice-cliff calving, may initiate the marine ice-cliff instability (MICI) if successive cliff-failure events expose increasingly thick ice as retreat proceeds inland (Extended Data Fig. 1). However, it is possible that changes to the terminus stress field, including buttressing from proglacial mélange[11–13], dynamic thinning[11,12,14], or variability in bed topography[11] will stabilize the cliff or even halt retreat altogether.

Ice-sheet models that include MICI represent the highest projections of future sea level rise[2,15], but the hypothesis remains controversial because self-sustaining retreat has never been directly observed, only inferred. Currently, two parameterizations of ice-cliff calving, which prescribe calving rates based on cliff height values, have been implemented in models that project future ice loss[2,12,16]. DeConto and Pollard[2,17] originally proposed that H_{crit} = 80–100 m based on theory

and limited observations, with calving rates ramping up from 0 to 3 km/a based on observations of the retreat of Sermeq Kujalleq (Jakosbhavn Isbrae) and Crane Glacier. When this parameterization is implemented, models predict the collapse of the West Antarctic Ice Sheet (WAIS), which contains 5 m of sea level equivalent, by 2300[2,15]. Recently, the application of a newer parameterization (H_{crit} = 135 m) based on a high-fidelity calving model by Crawford et al.[12] suggests that it is unlikely that WAIS collapses through a MICI-like mechanism in the 21st century[16]. These parameterizations, however, are limited by the paucity of observations associated with tall ice cliffs; the true value of H_{crit} and associated cliff-calving rates are not yet well known. Parameterizations of ice-cliff calving therefore remain poorly constrained, making the susceptibility of the ice sheets to MICI deeply uncertain, and contributing to the Intergovernmental Panel on Climate Change's *low-confidence* attribution to projections of future sea level rise[2,12]. Here we compile and analyze 15,015 observations of ice-cliff height around Antarctica and Greenland to empirically evaluate H_{crit}, the cliff-height stability limit. We find that ice-cliff calving occurs in diverse settings within the AIS and GrIS, and determine the rates and controls on retreat by this mechanism from additional remote sensing observations.

A new dataset of Earth's ice-cliff elevations

First, we combined data from airborne (Pre-IceBridge and Operation IceBridge, 2003–2019) and satellite (ICESat-2, 2018–2023) laser altimetry missions to determine ice-cliff positions and elevations across Antarctica and Greenland (Methods). The resulting cliff-height elevations in Fig. 1 show right-skewed, unimodal cliff-height distributions for both ice sheets. Only a handful of ice cliffs exist near the theoretical H_{crit} (~100 m)[1], providing observational support that H_{crit} is near or even below this value. In fact, in Antarctica, cliffs above just 52.2 m represent the 95th percentile boundary. The 95th percentile boundary in Greenland is 76.6 m. Remarkably, the AIS and GrIS contain very similar mean (31.3 m, 32.7 m) and maximum (123.7 m, 128.0 m) ice-cliff heights despite differences in their climatological and glaciological regimes.

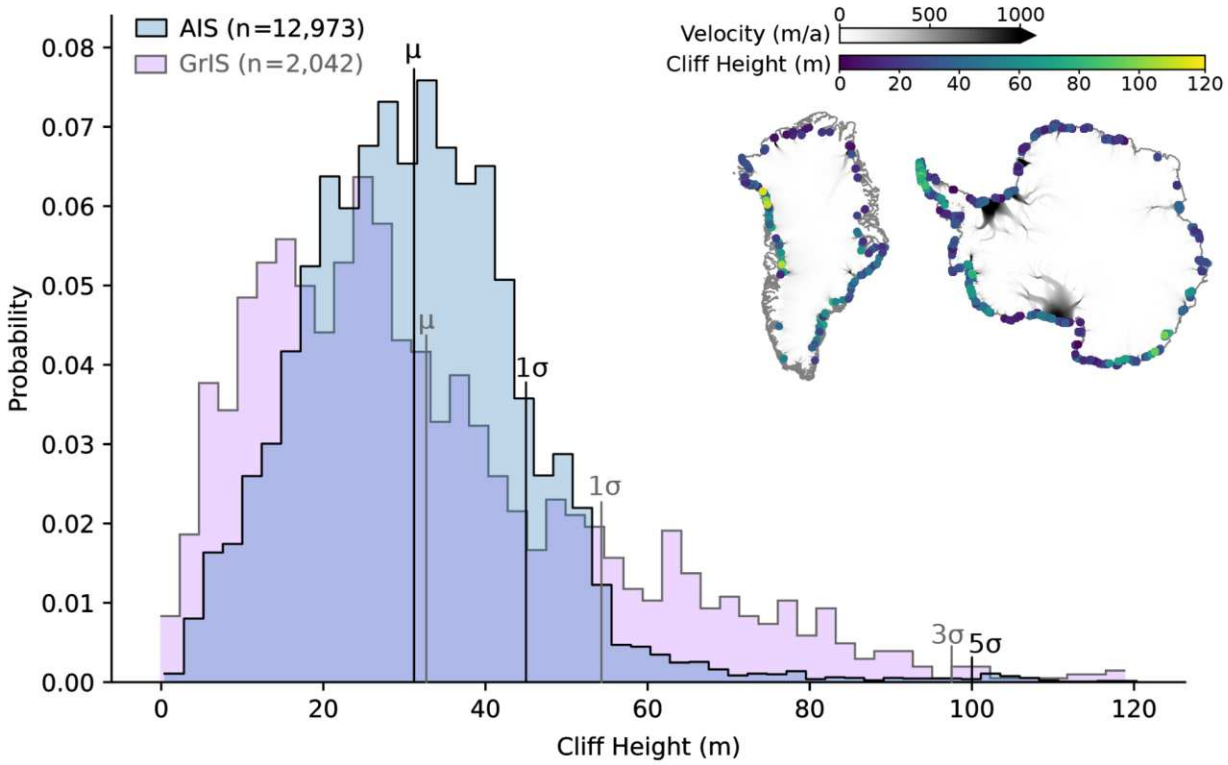

Fig. 1 | Ice-cliff heights in Antarctica and Greenland. Histogram of cliff-height datasets, with the dataset means (μ), and selected standard deviations (σ) labeled. The geographic distribution of each dataset is plotted over ice velocity[18,19] and the modern ice coastline[20,21] and colored by cliff height.

Controls on ice-cliff height

Next, we investigated potential controls on ice-cliff height by determining relationships between cliff height and parameters that may affect susceptibility to cliff failure, motivated by evidence from theory[1] and modeling[11,12,14]. We find that cliff height varies with both water depth and mélange thickness at the terminus, and the level of pre-existing 'damage' to the ice (Methods). Although climate forcings may act as triggers of individual calving events[22–24], we find no relationship between cliff-height and atmospheric temperature or sea surface temperature (Extended Data Fig 2).

We do find that cliff height generally increases with water depth (Figure 2), consistent with the theoretical expectation that increased hydrostatic pressure reduces the stress imbalance at a grounded ice cliff. We also find strong linear relationships between mean mélange thickness at the terminus and cliff height on both ice sheets (Figure 2). Buttressing from proglacial mélange, a granular mixture of calved icebergs and sea ice, may stabilize cliffs that would otherwise exceed H_{crit}, potentially arresting or preventing cliff failure entirely[11,12,25]. Here, mélange thickness measurements exclude large icebergs, which skew the mean mélange elevation (Methods). These data hint at a potential negative feedback within cliff-calving systems: thicker glacier cliffs calve thicker icebergs, which are more likely to anchor on the seafloor, leading to

enhanced sea ice development[26], and thus are more likely to be buttressed at their termini. However, the correlation between mélange thickness and cliff height might also simply exist because tall cliffs produce tall icebergs and, hence, thicker mélange.

During flow deformation, ice accumulates flaws that range from millimeter-scale microcracks[27–29] to meter-scale crevasses as the stress field evolves[30,31], which affect the stresses required for calving[6,11,14]. These flaws contribute to measurable topographic variations in the ice surface[32]. We use a simple parameter for topographic roughness as a proxy parameter for the level of pre-existing damage to the ice, where higher values of roughness correspond to larger or more spatially-dense flaws. We find that cliff height and damage exhibit a concave relationship on both ice sheets (Figure 2). Thicker cliffs are likely to be sites of elevated damage due to high stresses there, but we find that the very tallest cliffs are not the most damaged, implying that cliffs approaching H_{crit} may require more pristine ice with a higher effective yield strength to exist in such high-stress conditions. In other words, tall cliffs with high damage do not exist in large numbers, because high-stress, high-damage cliffs are likely to fail.

Together, systematic relationships between cliff height and water depth, mélange thickness, and damage provide observational links between ice cliffs and controls on their stability. Continent-wide trends imply that the tallest ice cliffs are likely to exist in deep water, with thick proglacial mélange, and relatively undamaged ice at the terminus.

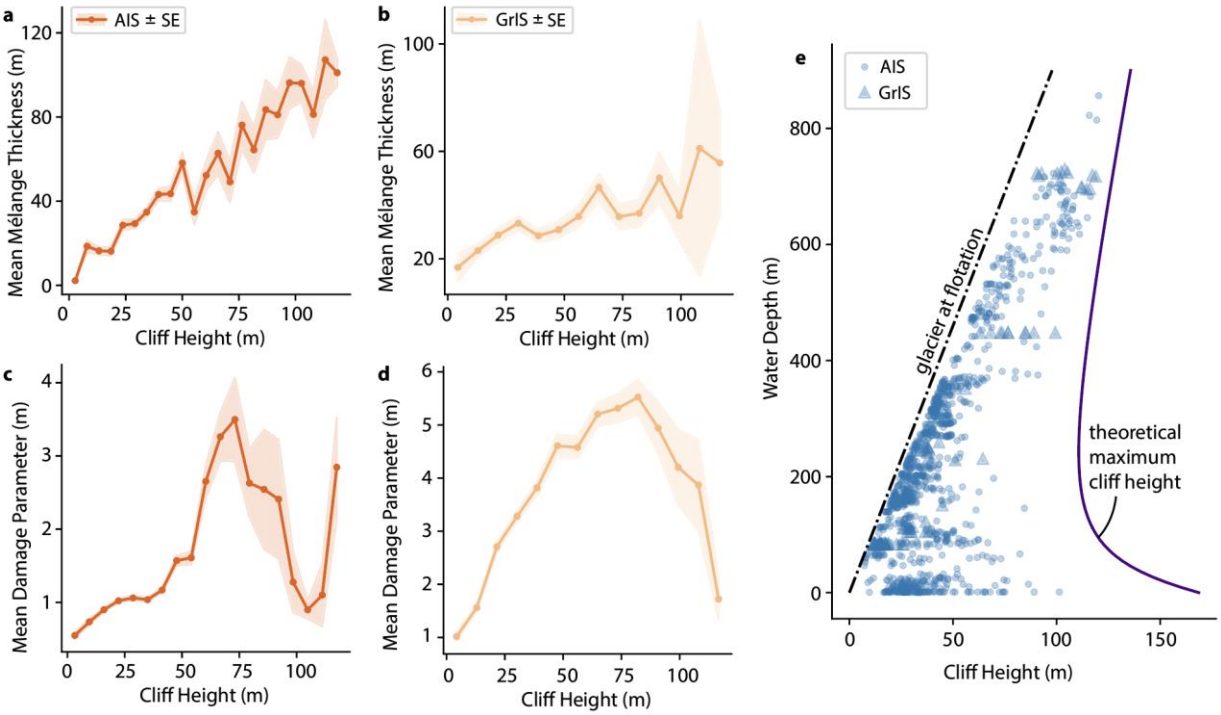

Fig. 2 | Relationships between mélange thickness, ice damage, water depth, and cliff height. (**a, b**) Relationship between binned means of cliff height and near-terminus mélange thickness in Antarctica (**a**) and Greenland (**b**). Shading denotes the standard error of the mean (SE). (**c, d**) Relationship between binned cliff height and our proxy for pre-existing damage (Methods) in Antarctica (**c**) and Greenland (**d**), with shading again denoting SE. (**e**) Grounded ice-cliff height plotted as a function of water depth[33,34] at the terminus. Data are bounded by the dashed line denoting thickness-depth combinations exactly at flotation and the solid line representing the theoretical maximum cliff height[1] (yield strength = 1 MPa; crevasse penetration ratio = 0.62), which shifts left with an assumed decrease in yield strength/increase in crevasse penetration and vice versa.

Observed rates of ice-cliff calving

Although continent-wide trends provide evidence for general controls on ice-cliff stability, ice-cliff failure is implemented in models by linking cliff height and calving rates at individual glaciers. We next focus on the tail of the cliff-height distribution (Figure 1) to investigate the dynamics of the tallest cliffs, where cliff failure is most likely to occur. We identify 16 glaciers with cliffs above 90 m during the study period (Figure 3). These locations are likely candidates for ice-cliff calving, given their cliff heights and in many cases "slump-uplift" features (see Figures 3e, 3f), which are distinct topographic signatures of cliff failure[6,11,12]. Of these 16 sites, four glaciers (Fleming Glacier, Commandant Charcot Glacier, Frost Glacier, Tuttulikassaap Sermia) benefit from high repeat sampling by ICESat-2 and undergo calving-front retreat during the study period (Extended Data Figs. 3–8). We estimate the calving rates (Methods) of these four glaciers to provide empirical constraints for the cliff-height calving-rate relationship.

When data from all four glaciers are taken together, cliff height and calving rate appear related during retreat, with more rapid rates generally associated with taller cliffs (Figure 3). Observed calving rates are much faster than existing parameterizations would predict based on cliff height alone (Figure 3). We find that ~100 m cliffs calve at more than triple the rate predicted by the DeConto and Pollard parameterization. The Crawford parameterization requires nearly double the observed cliff-height values to match observed calving rates, suggesting that the onset of cliff failure occurs in cliffs much shorter than 135 m. These data suggest that the application of either existing ice-cliff calving parameterization is likely to underestimate the contribution of the process to ice-sheet mass loss.

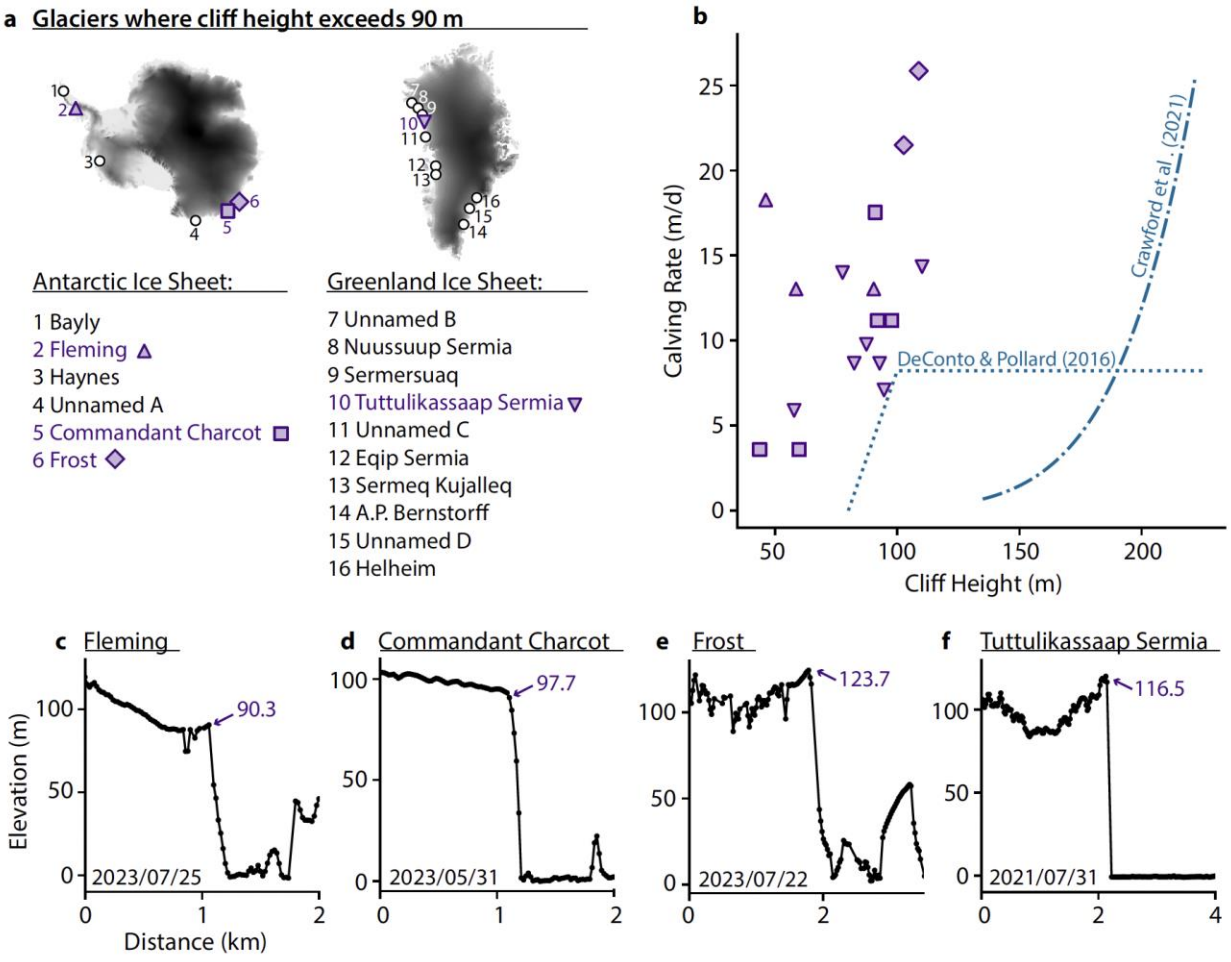

Fig. 3 | Observed rates of ice-cliff calving during retreat. (**a**) Maps of the 16 glaciers where cliffs exceed 90 m during the survey, with glaciers where calving rates are reported colored purple. (**b**) Calving rates during retreat plotted against associated cliff height observations for the selected glaciers, along with existing parameterizations for ice-cliff calving. Examples of cliff-height observations from altimetry profiles at Fleming (**c**), Commandant Charcot (**d**), Frost (**e**), and Tuttulikassaap Sermia (**f**).

Suppression of ice-cliff calving

Although rapid retreat by ice-cliff failure appears underway in Greenland and Antarctica, we find no evidence for runaway, MICI-style retreat. This is because rapid calving rates are not sustained throughout the survey period, and are either punctuated by periods of little-to-no calving or clearly decoupled from cliff-height increases (Extended Data Fig. 3). We see that ice-cliff failure eventually results in the advance of cliffs that either do not increase in height or thin rapidly (Extended Data Fig. 4). We investigate why cliffs that are perched near H_{crit} and retreat by ice-cliff failure do not undergo runaway retreat by examining the forces that lead to calving-cliff height change.

To achieve MICI, upstream thickening of an ice cliff must outpace dynamic thinning of the cliff, leading to the exposure of increasingly tall cliffs during retreat. Thickening, or an increase to the ice-cliff height, is accomplished by retreat into thicker ice upstream, and is therefore a function of the calving rate and the ice thickness gradient. Dynamic thinning of a cliff is accomplished by viscous flow deformation and is a function of the ice strain rate and the terminal ice thickness (Supplementary Information). Ice cliffs with a high dynamic-thinning component and a low cliff-thickening component are less vulnerable to runaway retreat by cliff failure (MICI), because lowering of the cliff below H_{crit} is likely to eventually occur. Conversely, ice cliffs with a low dynamic-thinning component and a high cliff-thickening component are more vulnerable to the instability, because taller and taller cliffs are likely to be revealed during retreat. Using just four parameters: the calving rate, ice thickness, ice thickness gradient, and strain rate, we can assess the vulnerability of a glacier to unstable retreat by cliff failure (Methods, Supplementary Information). We next evaluate the stability of ice cliffs at Fleming Glacier, Frost Glacier, and Tuttulikassaap Sermia by estimating these parameters from observations. We exclude data from Commandant Charcot Glacier, because no direct measurements of bed topography exist there, which prevents the calculation of the ice thickness.

Our results highlight the key role of the ice thickness gradients in controlling sustained ice-cliff calving. We find that cliffs shorter than 100 m tend to have high cliff-thickening components, explained by their steep ice thickness gradients, coupled with low dynamic-thinning components (Figure 4). This explains how the ~100 m cliffs we observe initially formed: via retreat into rapidly thickening ice, unmitigated by dynamic thinning. But as cliffs increase in height, the dynamic-thinning component increases with ice thickness. This is why the tallest cliffs exhibit the highest cliff-thinning component values (Figure 4). Critically, we find that cliff-thickening component values are low for the tallest cliffs, because their ice thickness gradients are low (Figure 4). We also see evidence of thick proglacial mélange during retreat at all three glaciers (Extended Data Fig. 3), which may have buttressed the cliffs and further decreased cliff-thickening component values by reducing the calving rate.

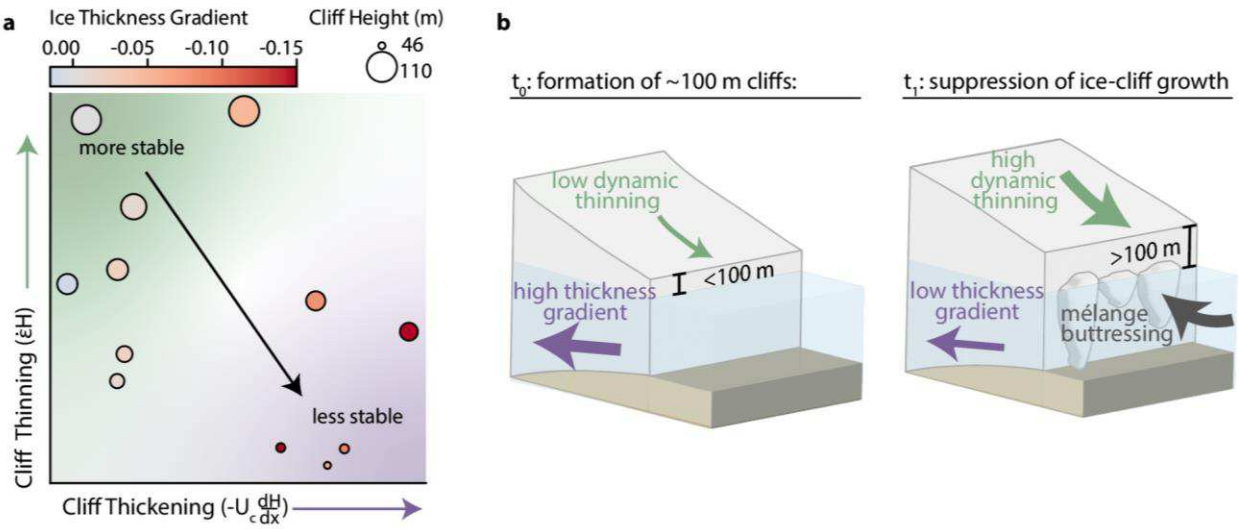

Fig. 4 | Controls on the initiation and suppression of ice-cliff calving. (a) Normalized ice-cliff thickening and thinning components based on observations of Fleming Glacier, Frost Glacier, and Tuttulikassaap Sermia (see Methods, Supplementary Information). Scatter sizes denote cliff height and colors denote ice-thickness gradient, with negative values referring to ice that thickens upstream. (b) Schematic representation of the processes that exposed ~100 m ice cliffs (time t_0; left) and suppressed further ice-cliff growth, preventing runaway retreat by MICI (time t_1; right).

The tallest cliffs we examine tend to exist in a stable configuration in relation to MICI, where the influence of dynamic thinning is high and the potential for upstream thickening is low. Together, these conditions prevented further cliff-thickening with retreat, explaining the eventual suppression of cliff-calving despite periods of rapid retreat.

Implications for ice-cliff instability

Our results reveal that although ice cliffs that exceed 100 m are rare, they do exist, and their dynamics provide empirical constraints on marine ice-cliff stability. The observations of ice-cliff calving presented here suggest that the process may occur much more rapidly than previously assumed. However, vulnerability to sustained cliff calving is highly sensitive to the ice thickness gradient, a finding consistent with previous modeling work[11].

We find that ~100 m cliffs were exposed by typical seasonal calving events and the removal of a non-buttressing[35] floating ice tongue (Extended Data Fig. 5). The vulnerability of the AIS to retreat by cliff failure is often discussed in the context of a future ice-sheet geometry that may exist after the hydrofracture-driven collapse of an ice shelf, which would likely reveal very tall cliffs[14,16]. Our results suggest that ice-shelf collapse is not a prerequisite for rapid cliff calving, and that retreat via other forms of calving is sufficient to trigger the process.

Nevertheless, the future collapse of a large ice shelf in West Antarctica may expose much taller cliffs than we report here[16]. Cliffs significantly taller than 100 m are likely to calve more rapidly

than the rates we observed but will likely also trigger a more rapid ice-flow acceleration (and associated dynamic thinning) than we observed (Extended Data Figs. 5–8)[36,37]. In our dataset, low ice thickness gradients upstream of ~100 m cliffs were insufficient to facilitate the sustained exposure of increasingly tall cliffs. There is no reason to believe that in the future, ~100 m cliffs elsewhere could not form in settings with much steeper upstream ice thickness gradients, creating conditions more vulnerable to MICI. Assessing the future susceptibility of Earth's ice sheets to MICI will require precise measurements of ice thickness gradients in vulnerable locations, as well as improved understanding of near-terminus ice rheology, which will dictate the magnitude of dynamic thinning in response to the formation of taller cliffs.

Methods

Ice cliff identification

We manually identified cliffs in altimetry data collected by the Ice, Cloud, and land Elevation Satellite-2 (ICESat-2), and the Operation IceBridge (OIB) and Pre-IceBridge (POIB) airborne missions. Ice, Cloud, and land Elevation Satellite (ICESat) altimetry data were not used in the survey to keep identifications to a manageable number while maximizing repeat observations along individual glaciers. ICESat-2 is equipped with the Advanced Topographic Laser Altimeter System (ATLAS), a photon-counting laser altimeter which collects ice surface elevation data every 0.7 m[38] with centimeter-scale accuracy[39]. The ICESat-2 profiles considered for cliff identification were limited to the period of four and a half years between 05/01/2019 – 10/01/2023, such that the ATLAS instrument was centered over each reference ground track (RGT), maximizing repeat acquisitions until the defined dataset end date. For Antarctica, cliff identification was limited to RGTs that intersect the ice coastline at approximately +/-45 degrees, which allowed for extraction of relevant local characteristics (e.g., mélange thickness, ice surface topography) while reasonably limiting the number of cliff identifications. The coastline-intersection criterion was relaxed for Greenland, where the orientations of narrow, fjord-constrained glaciers limit favorable intersections of ice fronts with ICESat-2. Here, we considered any intersection with the ice front valid for cliff identification. Data that failed the ATL06 quality control flag, and data with less than 200 photon returns in the area of interest (low data coverage) were excluded from the cliff survey.

We defined the cliff location as the elevation data point just before the break in slope that represents the ice cliff face. To correct ICESat-2 elevations and determine elevations as measured above the waterline (subaerial cliff height), we determined whether the cliff was likely to be grounded and applied corrections separately to floating and grounded cliffs. We determined the approximate grounding-state by calculating the height above floatation based on the bed elevation according to BedMachine[33,34,40,41]. When a cliff exceeded the theoretical height at floatation, (H_f):

$$H_f = b\left(1 - \frac{\rho_w}{\rho_i}\right)$$

we considered the cliff grounded, and the height above the EIGEN-6C4 geoid gives the height above the waterline (H_w). Where a cliff fell below H_f, we corrected for tidal fluctuations after Becker et al. (2021)[23] such that the tidally-corrected height is:

$$H_w = H_{cliff} - geoid - ot - dac - mdt$$

where H_{cliff} is the uncorrected cliff elevation, $geoid$ is the EIGEN-6C4 geoid height, ot is the ocean tide correction, dac is the dynamic atmospheric correction, and mdt is the mean dynamic topography correction.

NASA's POIB and OIB airborne missions collected data from 1993–2008 and 2009–2019 over the AIS and GrIS. Aircraft were equipped with Airborne Topographic Mapper (ATM), a laser altimeter that collected elevation data in a swath along the flight track[42,43]. ATM data are precise to the centimeter-scale and contain only sub-meter elevation biases[44]. All flight paths that intersect the modern ice-coastline were considered for cliff identification. Because tidal corrections are not provided in these datasets as they are in the ICESat–2 dataset, elevation data were simply corrected to the EIGEN-6C4 geoid to give the height of a cliff above the waterline.

One photogrammetric digital elevation model (DEM) produced from Maxar stereo-imagery and provided by the Polar Geospatial Center[45] was used to densify the cliff-height time series at Frost Glacier during retreat. Elevation was extracted from the DEM along the ICESat-2 RGT 0490 (beam 2r) and calibrated to ICESat-2 elevation data upstream.

Cliff-height errors

Height errors reported in the cliff-height dataset (as the variable H_{err}) are provided in the ICESat-2, OIB, and POIB datasets. The meaning of H_{err} varies due to measurement differences between platforms. For ICESat-2, H_{err} is the propagated error due to sampling error and the first photon bias correction from the land ice algorithm (h_li_sigma). For OIB and POIB, H_{err} is the RMS fit of the ATM data to the plane (rms_fit). In addition to these reported measurement errors, we performed quality flagging based on confidence in each manual cliff identification. Identification of cliff locations in altimetry data was not always trivial, especially in the presence of thick proglacial mélange, near-terminus rifts, and ice-shelf bending. These cases were flagged and are described further in the associated dataset description. Cases of dramatic upward ice-shelf bending, known as rampart-moats[23,46–48] were also flagged due to the effect of the rampart structure on the measured cliff height, which has resulted in a complementary Antarctic-wide catalogue of rampart-moat structures.

Characteristics of ice cliffs

We determined the mean mélange thickness by clipping each ICESat-2 profile used for cliff identification from the ice front (defined by the location of the ice cliff) to 1 km seaward of the front. The mean elevation from this 1 km profile gives a characteristic mélange height above the waterline when the presence of large icebergs, which heavily skew the along-profile mean elevation, are removed. After Meng et al. (2025)[49], elevations above 30 m are excluded from the mean mélange thickness calculation such that the elevation mean gives a mélange height

resulting from small icebergs and sea ice. To calculate mélange thickness from height, we assumed the mélange was in hydrostatic equilibrium. To produce Fig. 2a and 2b, ice cliffs and corresponding mean mélange thicknesses were separated into bins for approximately every 5 m of cliff height for the AIS and every 8.5 m of cliff height for the GrIS (due to the smaller dataset *n* there).

To quantify topographic roughness upstream of each ice cliff, we clipped each ICESat-2 profile used for cliff identification from the ice front to 500 m upstream (along-track) of the front. The clipped elevation profile was linearly detrended to remove the flow-related surface slope. The standard deviation of the detrended elevation profile was used as the proxy for damage in Fig. 2c and 2d. The plots were produced using the same cliff-height bins as the mean mélange thickness plots.

We investigated the influence of climate variables on cliff height using 2 m atmospheric temperature and sea surface temperature from the ERA5 global reanalysis dataset[50]. Data at each cliff location were annually averaged over the ICESat-2 survey period to calculate a characteristic mean temperature. These temperature data were binned in the same manner as the mélange thickness and damage variables to produce Extended Data Fig. 1. No point was plotted if all data within one bin were missing (NaN) in the reanalysis dataset. This likely occurred due to imperfect masking of the ice coastline in the reanalysis product.

Calving rates

We calculated calving rates (U_C) at Fleming Glacier, Commandant Charcot Glacier, Frost Glacier, and Tuttulikassaap Sermia glaciers using:

$$U_C = \underline{U_T} - \frac{dL}{dt},$$

where $\underline{U_T}$ is the vertically-averaged ice velocity, which we inferred from surface measurements, and $\frac{dL}{dt}$ is the change in glacier length over time, which we determined using ice-front position data. We traced ice-front positions in cloud-free Landsat-8/9 images at each case-study glacier, sampled approximately every 3 months to capture potential seasonality in calving-rate variability. For each glacier, we identified where each ice-front position crossed a reference centerline, which resulted in rates of advance and retreat along the glacier length $\left(\frac{dL}{dt}\right)$ in meters per day. Velocity data from the Inter-Mission Time Series of Land Ice Velocity and Elevation (ITS_LIVE) project, with annual data coverage through 2022, were used to calculate calving rates. Because calving rates beyond 2022 were of interest for all glaciers, the 2022 velocity data were used to calculate calving rates in 2023 and 2024. Given the temporal limitations of existing velocity data, variability in the availability of cloud-free imagery data, and the time-averaged nature of calving rate as a measurement, the calculated calving rates represent best-available estimates.

Ice thicknesses, thickness gradients, and strain rates

We examined the suppression of ice-cliff calving and vulnerability to MICI based on the rate of ice thickness change at a cliff, which is a function of the calving rate, ice thickness, ice thickness gradient, and strain rate (equation described in Supplementary Information).

Calving rate was calculated as described above. Ice thickness was calculated by subtracting the bed elevation (BedMachine) from the corrected ice-cliff height (ICESat-2). The ice thickness gradient was calculated by combining surface and bed slopes. Surface slope was calculated by taking the mean slope of the ICESat-2 elevation profile 1 km upstream of the terminus, and bed slope was calculated by taking the mean slope of the bed topography along the centerline for the region over which the glacier retreated during each calving-rate time window. Strain rate ($\dot{\varepsilon}$) was calculated using Glen's flow law, which assumes a power-law rheology for ice, written as

$$\dot{\varepsilon_e} = A\tau_e^n,$$

where $\dot{\varepsilon_e}$ is the effective strain rate, τ_e is the effective stress, A is a pre-factor, and n is the stress exponent. We estimated stress using an expression for the depth-averaged horizontal deviatoric stress (τ_{xx}) based on the force balance at an ice cliff[51]:

$$\tau_{xx} = \frac{\rho_i g H}{4}\left(1 - \frac{\rho_w}{\rho_i}\left(\frac{D}{H}\right)^2\right),$$

where ρ_i and ρ_w are the densities of ice (910 kg/m^3) and seawater (1020 kg/m^3), D is the water depth, H is the ice thickness, and g is the gravitational constant. We assume that the rheological parameters in the flow law (A, n) do not vary among the three glaciers we examined using this method, which allowed us to avoid prescribing exact values for A and n, which are a subject of longstanding debate. We therefore normalized the dynamic-thinning and cliff-thickening components, which revealed the glacier-to-glacier trend in component values, rather than exact values for the rates of dynamic thinning or cliff thickening.

References

1. Bassis, J. N. & Walker, C. C. Upper and lower limits on the stability of calving glaciers from the yield strength envelope of ice. *Proc. R. Soc. A.* **468**, 913–931 (2012).
2. DeConto, R. M. & Pollard, D. Contribution of Antarctica to past and future sea-level rise. *Nature* **531**, 591–597 (2016).
3. Wise, M. G., Dowdeswell, J. A., Jakobsson, M. & Larter, R. D. Evidence of marine ice-cliff instability in Pine Island Bay from iceberg-keel plough marks. *Nature* **550**, 506–510 (2016).
4. Joughin, I., Shean, D. E., Smith, B. E. & Floricioiu, D. A decade of variability on Jakobshavn Isbræ: ocean temperatures pace speed through influence on mélange rigidity. *The Cryosphere* **14**, 211–227 (2020).
5. Needell, C. & Holschuh, N. Evaluating the Retreat, Arrest, and Regrowth of Crane Glacier Against Marine Ice Cliff Process Models. *Geophysical Research Letters* **50**, e2022GL102400 (2023).
6. Parizek, B. R. *et al.* Ice-cliff failure via retrogressive slumping. *Geology* **47**, 449–452 (2019).
7. Ma, Y., Tripathy, C. S. & Bassis, J. N. Bounds on the calving cliff height of marine terminating glaciers. *Geophysical Research Letters* **44**, 1369–1375 (2017).
8. Weertman, J. Stability of the Junction of an Ice Sheet and an ice Shelf. *Journal of Glaciology* **13**, (1974).
9. Bassis, J. N. *et al.* Stability of Ice Shelves and Ice Cliffs in a Changing Climate. *Annu. Rev. Earth Planet. Sci.* **52**, annurev-earth-040522-122817 (2024).
10. Paolo, F. S., Fricker, H. A. & Padman, L. Volume loss from Antarctic ice shelves is accelerating. *Science* **348**, 327–331 (2015).
11. Bassis, J. N., Berg, B., Crawford, A. J. & Benn, D. I. Transition to marine ice cliff instability controlled by ice thickness gradients and velocity. *Science* **372**, 1342–1344 (2021).
12. Crawford, A. J. *et al.* Marine ice-cliff instability modeling shows mixed-mode ice-cliff failure and yields calving rate parameterization. *Nat Commun* **12**, 2701 (2021).
13. Schlemm, T. & Levermann, A. A simple parametrization of mélange buttressing for calving glaciers. *The Cryosphere* **15**, 531–545 (2021).
14. Clerc, F., Minchew, B. M. & Behn, M. D. Marine Ice Cliff Instability Mitigated by Slow Removal of Ice Shelves. *Geophys. Res. Lett.* **46**, 12108–12116 (2019).
15. DeConto, R. M. *et al.* The Paris Climate Agreement and future sea-level rise from Antarctica. *Nature* **593**, 83–89 (2021).
16. Morlighem, M. *et al.* The West Antarctic Ice Sheet may not be vulnerable to marine ice cliff instability during the 21st century. *Sci. Adv.* **10**, eado7794 (2024).
17. Pollard, D., DeConto, R. M. & Alley, R. B. Potential Antarctic Ice Sheet retreat driven by hydrofracturing and ice cliff failure. *Earth and Planetary Science Letters* **412**, 112–121 (2015).
18. Joughin, I., Smith, B., Howat, I. & Scambos, T. MEaSUREs Greenland Ice Sheet Velocity Map from InSAR Data, Version 2. NASA National Snow and Ice Data Center Distributed Active Archive Center https://doi.org/10.5067/OC7B04ZM9G6Q (2015).
19. Rignot, E., Mouginot, J. & Scheuchl, B. MEaSUREs InSAR-Based Antarctica Ice Velocity Map, Version 2. NASA National Snow and Ice Data Center Distributed Active Archive Center https://doi.org/10.5067/D7GK8F5J8M8R (2017).
20. Gerrish, L. The coastline of Kalaallit Nunaat/ Greenland available as a shapefile and geopackage, covering the main land and islands, with glacier fronts updated as of 2017. 2 files, 5.26 MB UK Polar Data Centre, Natural Environment Research Council, UK Research & Innovation https://doi.org/10.5285/8CECDE06-8474-4B58-A9CB-B820FA4C9429 (2020).
21. Gerrish, L., Ireland, L., Fretwell, P. T. & Cooper, P. High resolution vector polylines of the Antarctic coastline - VERSION 7.10. 2 files, 162 MB NERC EDS UK Polar Data Centre https://doi.org/10.5285/567C0911-83A0-493C-9DC7-15245C1C5F5E (2024).
22. Bassis, J. N. & Ma, Y. Evolution of basal crevasses links ice shelf stability to ocean forcing. *Earth and Planetary Science Letters* **409**, 203–211 (2015).

23. Becker, M. K. *et al.* Buoyancy-Driven Flexure at the Front of Ross Ice Shelf, Antarctica, Observed With ICESat-2 Laser Altimetry. *Geophysical Research Letters* **48**, e2020GL091207 (2021).
24. Banwell, A. F., MacAyeal, D. R. & Sergienko, O. V. Breakup of the Larsen B Ice Shelf triggered by chain reaction drainage of supraglacial lakes. *Geophysical Research Letters* **40**, 5872–5876 (2013).
25. Schlemm, T., Feldmann, J., Winkelmann, R. & Levermann, A. *Stabilizing Effect of Mélange Buttressing on the Marine Ice Cliff Instability of the West Antarctic Ice Sheet*. https://tc.copernicus.org/preprints/tc-2021-238/ (2021) doi:10.5194/tc-2021-238.
26. Fraser, A. D., Massom, R. A., Michael, K. J., Galton-Fenzi, B. K. & Lieser, J. L. East Antarctic Landfast Sea Ice Distribution and Variability, 2000–08. *Journal of Climate* **25**, 1137–1156 (2012).
27. Gold, L. W. The cracking activity in ice during creep. *Can. J. Phys.* **38**, 1137–1148 (1960).
28. Sinha, N. K. Intercrystalline cracking, grain-boundary sliding, and delayed elasticity at high temperatures. *J Mater Sci* **19**, 359–376 (1984).
29. Frost, H. J. Mechanisms of crack nucleation in ice. *Engineering Fracture Mechanics* **68**, 1823–1837 (2001).
30. van der Veen, C. J. Crevasses on glaciers 1. *Polar Geography* **23**, 213–245 (1999).
31. Colgan, W. *et al.* Glacier crevasses: Observations, models, and mass balance implications. *Reviews of Geophysics* **54**, 119–161 (2016).
32. Watkins, R. H., Bassis, J. N. & Thouless, M. D. Roughness of Ice Shelves Is Correlated With Basal Melt Rates. *Geophysical Research Letters* **48**, e2021GL094743 (2021).
33. Morlighem, M. *et al.* Deep glacial troughs and stabilizing ridges unveiled beneath the margins of the Antarctic ice sheet. *Nat. Geosci.* **13**, 132–137 (2020).
34. Morlighem, M. *et al.* BedMachine v3: Complete Bed Topography and Ocean Bathymetry Mapping of Greenland From Multibeam Echo Sounding Combined With Mass Conservation. *Geophysical Research Letters* **44**, 11,051-11,061 (2017).
35. Gudmundsson, G. H. Ice-shelf buttressing and the stability of marine ice sheets. *The Cryosphere* **7**, 647–655 (2013).
36. Scambos, T. A. Glacier acceleration and thinning after ice shelf collapse in the Larsen B embayment, Antarctica. *Geophys. Res. Lett.* **31**, L18402 (2004).
37. Dupont, T. K. & Alley, R. B. Assessment of the importance of ice-shelf buttressing to ice-sheet flow. *Geophysical Research Letters* **32**, (2005).
38. Smith, B. *et al.* ATLAS/ICESat-2 L3A Land Ice Height, Version 6. NASA National Snow and Ice Data Center Distributed Active Archive Center https://doi.org/10.5067/ATLAS/ATL06.006 (2023).
39. Brunt, K. M., Neumann, T. A. & Smith, B. E. Assessment of ICESat-2 Ice Sheet Surface Heights, Based on Comparisons Over the Interior of the Antarctic Ice Sheet. *Geophysical Research Letters* **46**, 13072–13078 (2019).
40. Morlighem, M. MEaSUREs BedMachine Antarctica, Version 3. NASA National Snow and Ice Data Center Distributed Active Archive Center https://doi.org/10.5067/FPSU0V1MWUB6 (2020).
41. Morlighem, M. IceBridge BedMachine Greenland, Version 5. NASA National Snow and Ice Data Center Distributed Active Archive Center https://doi.org/10.5067/GMEVBWFLWA7X (2022).
42. Studinger, M. IceBridge ATM L2 Icessn Elevation, Slope, and Roughness, Version 2. (2014).
43. Thomas, R. & Studinger, M. Pre-IceBridge ATM L2 Icessn Elevation, Slope, and Roughness, Version 1. (2010).
44. Brunt, K. M. *et al.* Assessment of NASA airborne laser altimetry data using ground-based GPS data near Summit Station, Greenland. *The Cryosphere* **11**, 681–692 (2017).
45. Howat, I. *et al.* The Reference Elevation Model of Antarctica - Strips, Version 4.1. Harvard Dataverse https://doi.org/10.7910/DVN/X7NDNY (2022).
46. Scambos, T., Sergienko, O., Sargent, A., MacAyeal, D. & Fastook, J. ICESat profiles of tabular iceberg margins and iceberg breakup at low latitudes. *Geophysical Research Letters* **32**, (2005).
47. Wagner, T. J. W., James, T. D., Murray, T. & Vella, D. On the role of buoyant flexure in glacier calving. *Geophysical Research Letters* **43**, 232-240A (2016).

48. Wagner, T. J. W. *et al.* The “footloose” mechanism: Iceberg decay from hydrostatic stresses. *Geophysical Research Letters* **41**, 5522–5529 (2014).
49. Meng, Y. *et al.* Seasonal changes of mélange thickness coincide with Greenland calving dynamics. *Nat Commun* **16**, 573 (2025).
50. Hersbach, H. *et al.* The ERA5 global reanalysis. *Quarterly Journal of the Royal Meteorological Society* **146**, 1999–2049 (2020).
51. Van der Veen, C. J. Tidewater calving. *Journal of Glaciology* **42**, 375–385 (1996).

Data Availability

All ICESat-2, Pre-IceBridge, and Operation IceBridge data used in this study are freely available to download from the National Snow and Ice Data Center at: https://doi.org/10.5067/ATLAS/ATL06.006, https://doi.org/10.5067/CPRXXK3F39RV, and https://doi.org/10.5067/6C6WA3R918HJ, respectively. We use bed elevations from BedMachine Antarctica v3 (https://doi.org/10.5067/FPSU0V1MWUB6) and Bedmachine Greenland v5 (https://doi.org/10.5067/GMEVBWFLWA7X). We use surface velocities from ITS_LIVE (Antarctic data available at https://doi.org/10.5067/9ZFX84T5GI6D and Greenland data at https://doi.org/10.5067/579TO87M7IZB) and imagery data from the Landsat 8-9 catalogue (https://doi.org/10.5066/P975CC9B) to estimate calving rates. The final, processed cliff-height dataset, including height errors, related derived products (such as mélange thickness, damage parameter, ice front position, and calving rate data), and dataset descriptions will be made publicly available by the time of publication.

Code Availability

Code that reproduces the figures in the main text will be made publicly available by the time of publication.

Acknowledgements

C.N., C.C.W., and J.N.B. acknowledge funding from NASA Award 80NSSC22K0380. C.N. was also supported by the NSF GRFP. C.C.W. was also supported by NASA grant 80NSSC22K0547. J.N.B was also funded by DoE grant C3710, Framework for Antarctic System Science in E3SM, NASA grant 80NSSC22K0378 and by the DOMINOS project, a component of the International Thwaites Glacier Collaboration (ITGC). Support from National Science Foundation (NSF: Grant 1738896), Natural Environment Research Council (NERC: Grant NE/S006605/1), and NASA grant 80NSSC20K0568. We thank the Polar Geospatial Center for providing the DEM generated from Maxar imagery over Frost Glacier used to densify the cliff-height time series.

Author Contributions

C.C.W. and J.N.B. acquired the funding. All authors contributed to conceptualizing the study. C.N. collected and analyzed the data, produced the figures, and wrote the initial manuscript draft under C.C.W's supervision. All authors contributed to interpreting results and writing and editing the manuscript.

Competing Interests

The authors declare no competing financial interests.

Correspondence and requests for materials should be addressed to Caroline Needell.

Extended Data Figures

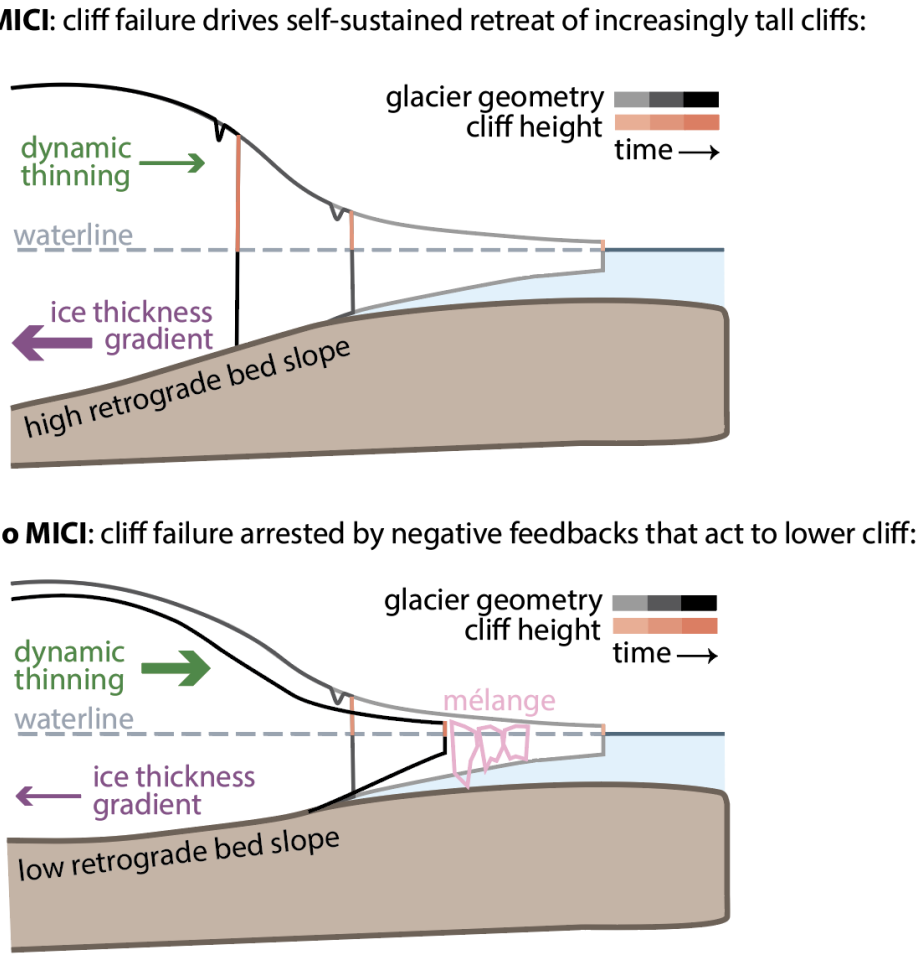

Extended Data Figure 1 | Schematic diagram of marine ice-cliff instability. (**a**) Conditions that may lead to self-sustaining retreat by MICI, as increasingly tall cliffs form during retreat. Here, increases to the cliff height outpace dynamic thinning. (**b**) Conditions that may lead to suppression of ice-cliff failure. A lower bed slope or ice thickness gradient may allow dynamic thinning to lower the cliff height below the critical height, facilitating advance. Mélange buttressing may also suppress calving by stabilizing the cliff.

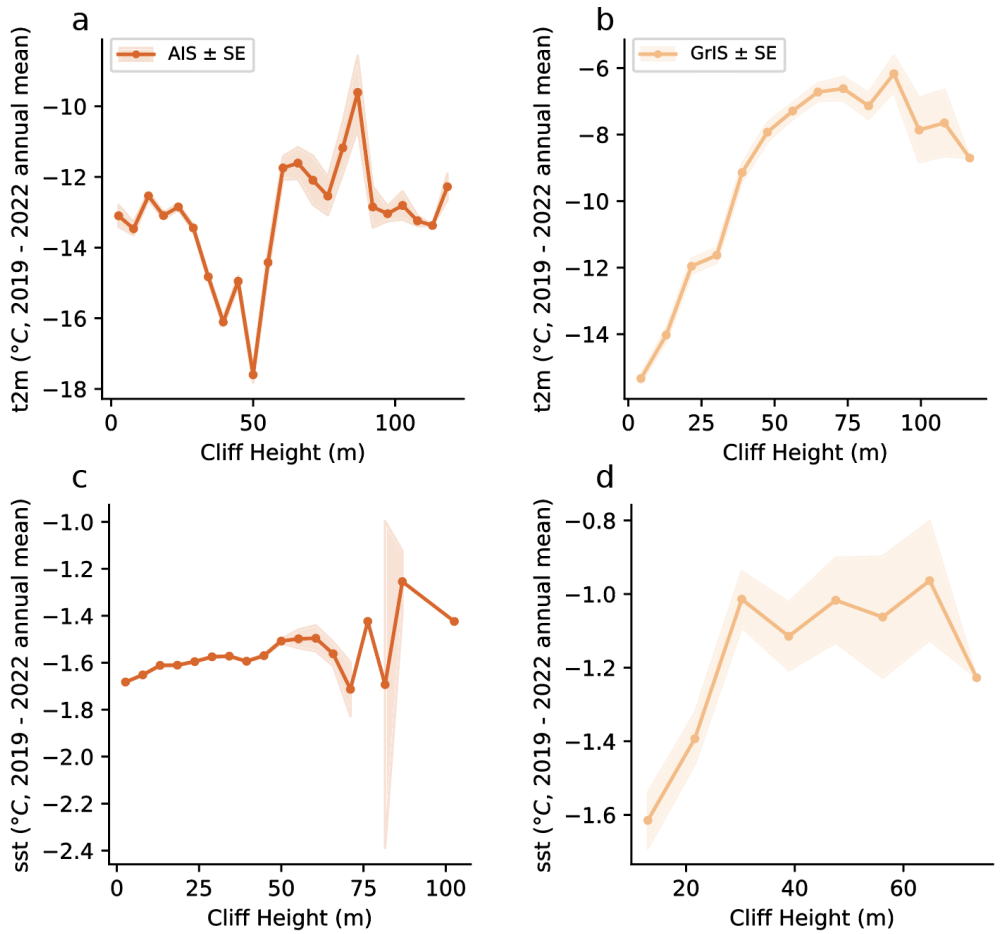

Extended Data Figure 2 | Relationships between climate forcing and cliff height. (**a, b**) Show the relationship between binned cliff height and mean annual 2 m temperature (t2m) for the ICESat-2 cliff survey period from ERA5 reanalysis data in Antarctica (**a**) and Greenland (**b**) **(c,d)** show the relationship between binned cliff height and mean annual sea surface temperature (sst) for the same period. The binned means are plotted in solid color, with shading denoting the standard error of the mean.

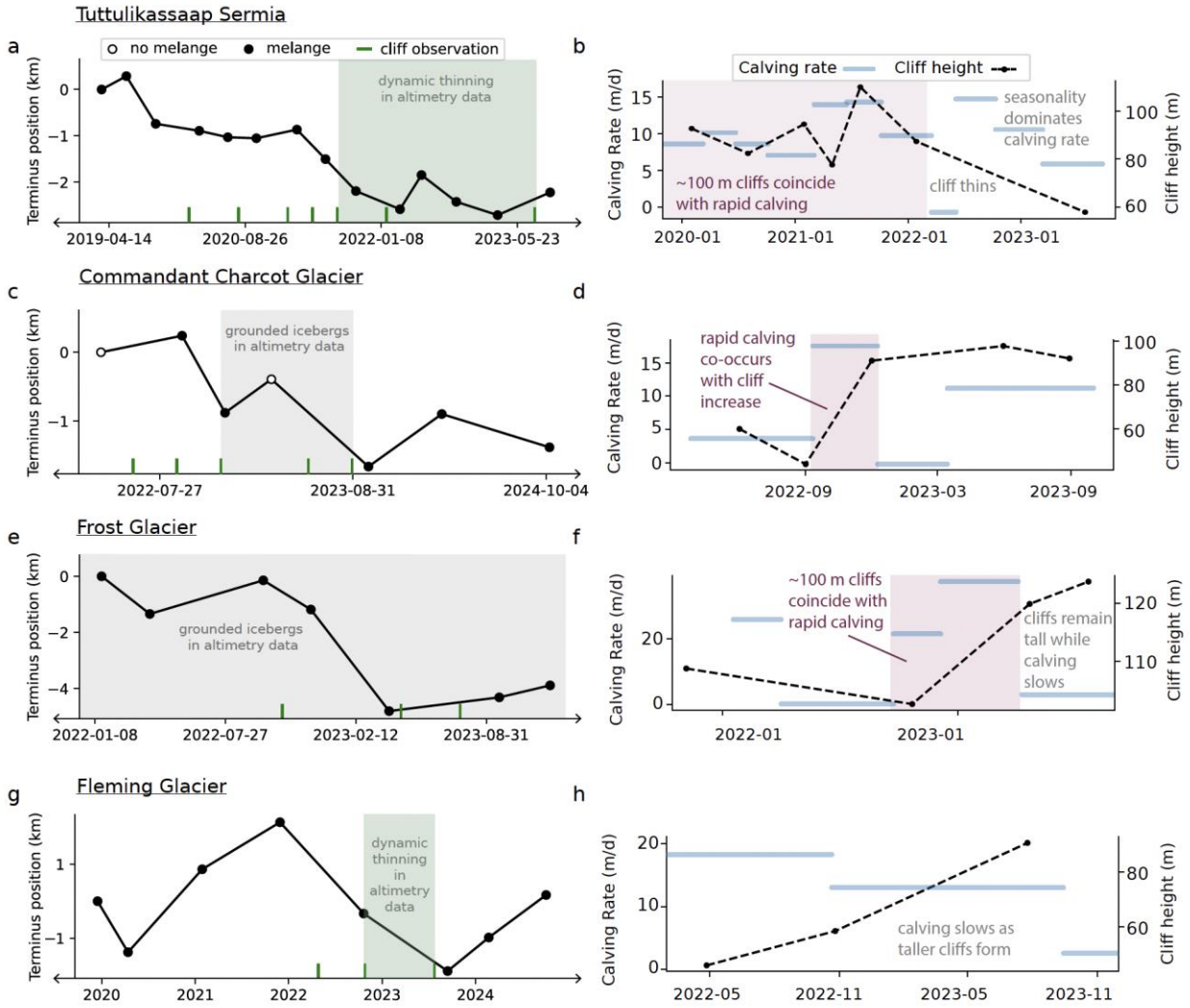

Extended Data Figure 3 | Timing of terminus retreat, calving rate, and cliff height observations. Terminus evolution plotted through time for **(a)** Tuttulikassaap Sermia, **(c)** Commandant Charcot Glacier, **(e)** Frost Glacier, and **(g)** Fleming Glacier, with the initial position plotted at 0 km and retreat (advance) represented by negative (positive) slope. Terminus positions are derived from ice-fronts identified from Landsat 8/9 images, with filled circles denoting mélange present in imagery data and empty circles denoting no mélange. Green ticks show timing of cliff observations, and shaded regions denote periods of grounded iceberg presence and near-terminus thinning in altimetry data. Cliff-height through time (black dashed) and best known time-averaged calving-rates (blue) are shown for **(b)** Tuttulikassaap Sermia, **(d)** Commandant Charcot Glacier, **(f)** Frost Glacier, and **(h)** Fleming Glacier. Pink annotations on calving-rate panels highlight periods of potential coupling between cliff-height and calving rate, and grey annotations denote periods where cliff-height and calving rate are decoupled.

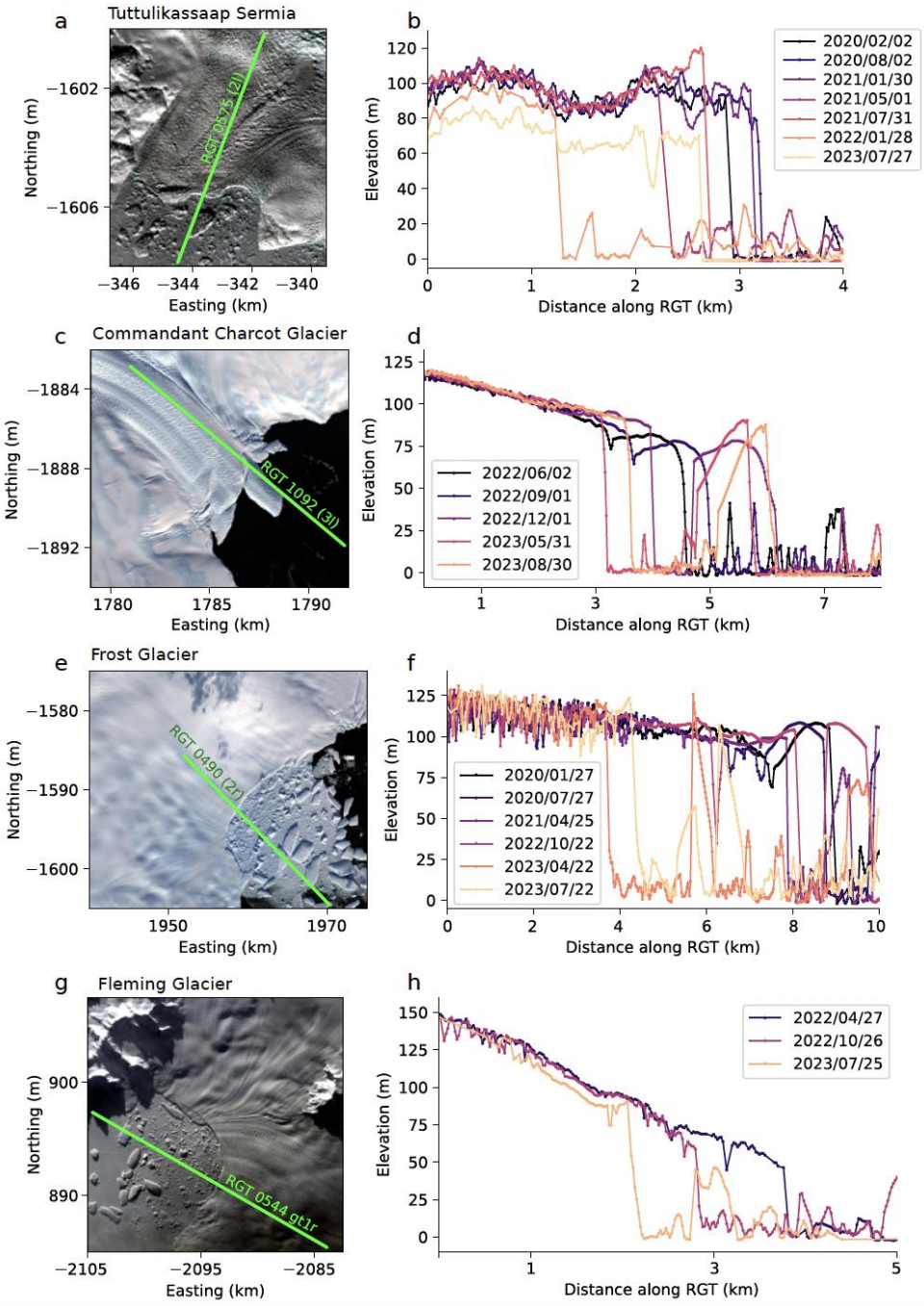

Extended Data Figure 4 | ICESat-2 tracks and full altimetry time-series data for case-study glaciers. ICESat-2 reference ground track coordinates shown over Landsat-8/9 images, and all corresponding usable ICESat-2 altimetry profiles plotted along the ground track during the cliff survey period for **(a, b)** Tuttulikassaap Sermia, **(c, d)** Commandant Charcot Glacier, **(e, f)** Frost Glacier, and **(g, h)** Fleming Glacier.

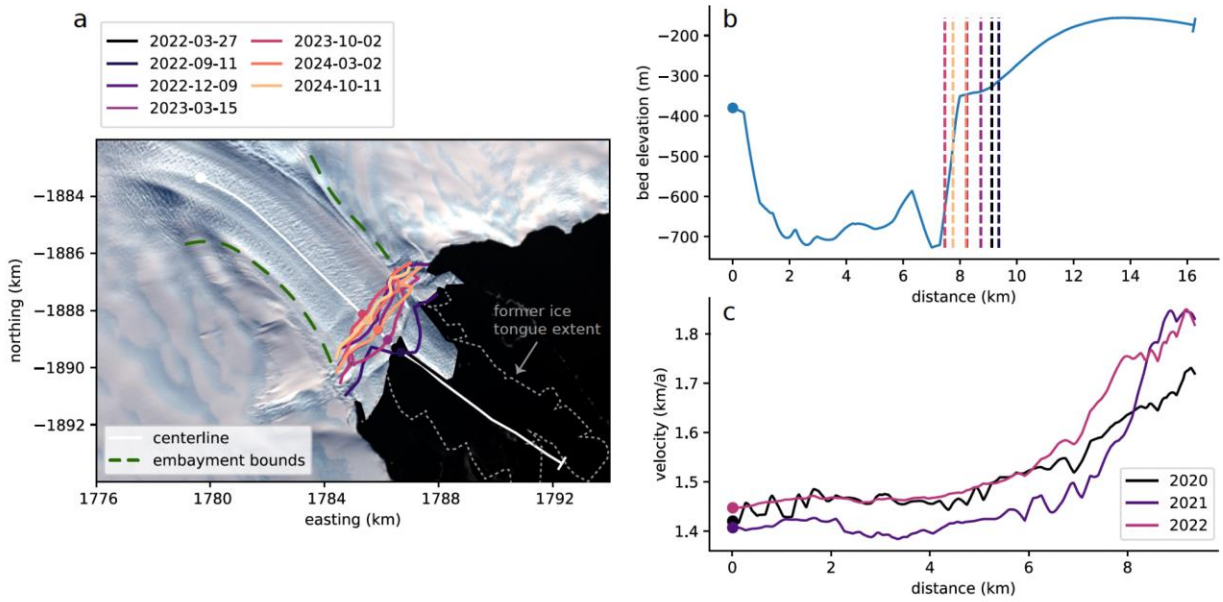

Extended Data Figure 5 | Commandant Charcot Glacier glaciological context. (a) Ice front positions through time, centerline used to calculate calving rates, and approximate embayment bounds. The former ice tongue extent (gray dotted), which calved in early 2022, is also shown. **(b)** Bed elevation along centerline, with ice front positions though time plotted as dashed lines. (**c**) Velocity profiles along the centerline through time.

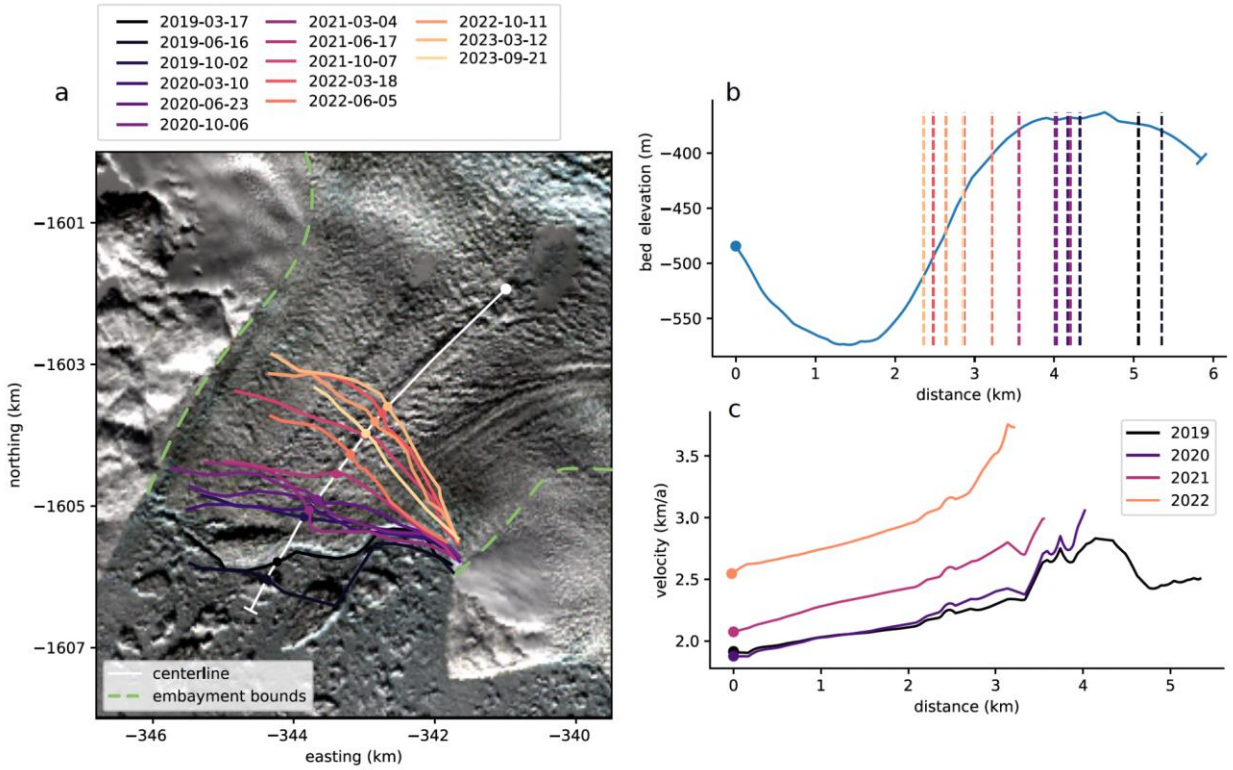

Extended Data Figure 6 | Tuttulikassaap Sermia glaciological context. (a) Ice front positions through time, centerline used to calculate calving rates, and approximate embayment bounds. **(b)** Bed elevation along centerline, with ice front positions though time plotted as dashed lines. (**c**) Velocity profiles along the centerline through time.

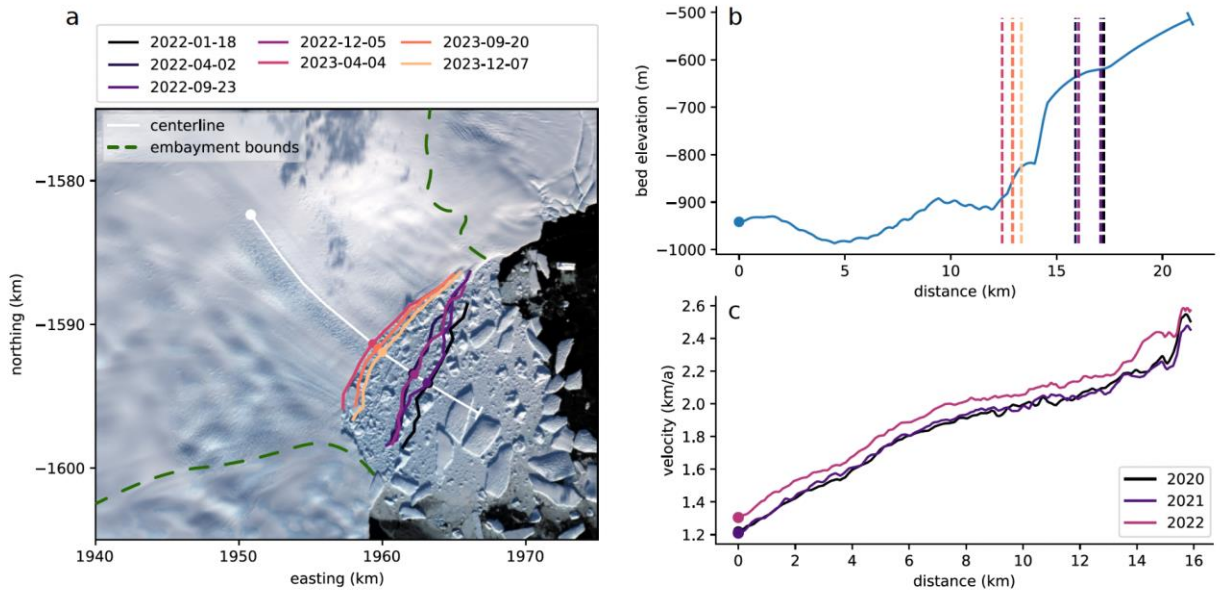

Extended Data Figure 7 | Frost Glacier glaciological context. (a) Ice front positions through time, centerline used to calculate calving rates, and approximate embayment bounds. **(b)** Bed elevation along centerline, with ice front positions though time plotted as dashed lines. (**c**) Velocity profiles along the centerline through time.

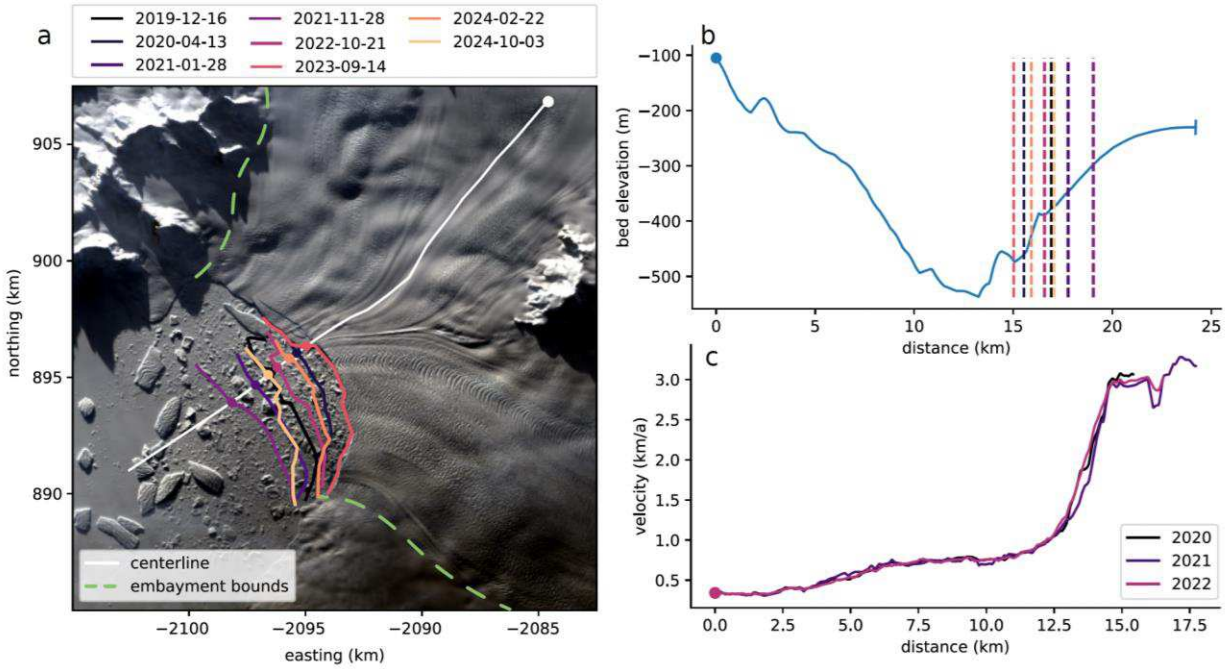

Extended Data Figure 8 | Fleming Glacier glaciological context. (a) Ice front positions through time, centerline used to calculate calving rates, and approximate embayment bounds. **(b)** Bed elevation along centerline, with ice front positions though time plotted as dashed lines. (**c**) Velocity profiles along the centerline through time.

Supplementary Files

This is a list of supplementary files associated with this preprint. Click to download.

- supplementaryinformationfinal.docx